ACS NANO

www.acsnano.org

ARTICLE

Patternable Process-Induced Strain in 2D Monolayers and Heterobilayers

Yue Zhang, ▽ M. Abir Hossain, ▽ Kelly J. Hwang, ▽ Paolo F. Ferrari, Joseph Maduzia, Tara Peña, Stephen M. Wu, Elif Ertekin, and Arend M. van der Zande*

Cite This: https://doi.org/10.1021/acsnano.3c09354

ABSTRACT: **Strain engineering in two-dimensional (2D) materials is a powerful but difficult to control approach to tailor material properties. Across applications, there is a need for device-compatible techniques to design strain within 2D materials. This work explores how process-induced strain engineering, commonly used by the semiconductor industry to enhance transistor performance, can be used to pattern complex strain profiles in monolayer MoS_2 and 2D heterostructures. A traction−separation model is identified to predict strain profiles and extract the interfacial traction coefficient of 1.3 ± 0.7 MPa/μm and the damage initiation threshold of 16 ± 5 nm. This work demonstrates the utility to (1) spatially pattern the optical band gap with a tuning rate of 91 ± 1 meV/% strain and (2) induce interlayer heterostrain in MoS_2−WSe_2 heterobilayers. These results provide a CMOS-compatible approach to design complex strain patterns in 2D materials with important applications in 2D heterogeneous integration into CMOS technologies, moiré engineering, and confining quantum systems.**

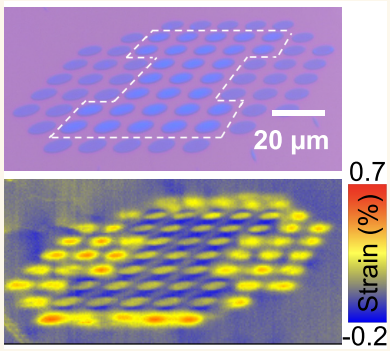

KEYWORDS: *2D materials, nanomechanics, strain engineering, optical spectroscopy, interfacial mechanics*

Strain often plays an unknown but important role in nanoscale materials properties and device behavior. Two-dimensional (2D) van der Waals (vdW) materials like graphene or transition metal dichalcogenides (e.g., MoS_2, WSe_2) are ideal ultrastrength materials that host rich strain-induced behavior[1] and where bringing deterministic design to strain will have both technological and scientific impact. For example, while 2D materials are considered contenders to extend transistor scaling or post-Moore's law technology, a current challenge is the heterogeneous integration of 2D materials with complementary metal-oxide-semiconductor (CMOS)-compatible processes and unraveling how these processes impact strain and doping.[2,3] Simultaneously, 2D materials exhibit exciting but difficult to control strain phenomena such as band gap tuning,[4,5] electron mobility enhancement,[6] directing or confining excitons,[7−12] superlattices,[13,14] single-photon emitters,[15−19] phase changes,[20−22] pseudomagnetic fields,[23−26] and magnetism.[27−29] Mechanically, 2D layers can withstand large strains before fracture (>10% for MoS_2[30]), and the vdW bonding allows slip at the interface with the substrate or between layers.[31−33] The fundamental studies above typically introduce strain via external manipulation such as nanoindentation,[34] electrostatic tensioning,[35] transferring onto nanotemplates,[36,37] nanorods,[15] trapped gases in micro/nanoballoons,[9,23,38−40] macroscale bending on soft substrates,[4,6,41] or self-assembly via nanoscale wrinkling.[42−46] To fully leverage the power of strain engineering in 2D materials across all applications, fabrication approaches and models are needed to predict, design, and pattern strain on the nanoscale.

A recent trend has been to apply the decades-old process-induced strain technique used by the semiconductor industry[47−52] to 2D materials. Process-induced strain by depositing high-stress thin films (stressors) is a powerful approach for engineering strain at the nanoscale and is widely used in CMOS processes for mobility enhancement in silicon transistors. These stressors can apply significant thin film forces > 20 N/m onto the underlying substrate. When applied to 2D multilayers, depositing stressors leads to large anisotropic strains[53,54] and interlayer slip.[55] While promising, the previous results are primarily performed on multilayers, where Raman signals are averaged through every layer. Thus, it is difficult to quantify or deconvolve the contributions from strain, doping, and layer number. Nor did the previous works develop models

Received: September 26, 2023
Revised: January 16, 2024
Accepted: January 18, 2024

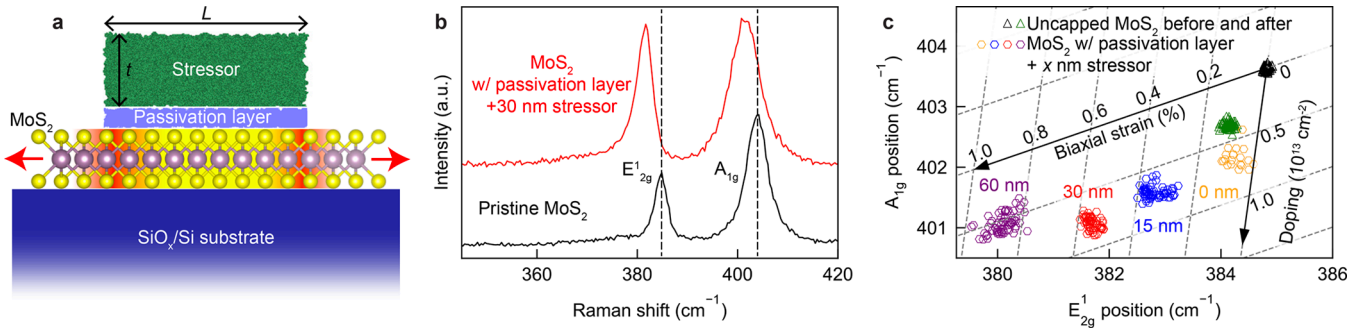

Figure 1. (a) Schematic cross-sectional view showing a patterned stack consisting of a passivation layer and stressor deposited on monolayer MoS_2 on a SiO_x/Si substrate. (b) Raman spectra of pristine MoS_2 (black) and after capping by a passivation layer and 30 nm thick stressor (red). (c) Scatter plot of MoS_2 Raman E^1_{2g} and A_{1g} mode positions, for uncapped MoS_2 before (black triangle) and after (green triangle) the deposition, and MoS_2 capped by the 6 nm Al_2O_x passivation layer and MgO_x stressor of increasing thicknesses of 0 nm (orange), 15 nm (blue), 30 nm (red), and 60 nm (purple).

to understand the spatially heterogeneous in-plane strains. The key step to deterministic strain engineering in 2D materials is to quantify the strain transfer in monolayers, discover the interfacial mechanics governing the behavior, and identify how the strain influences the material structure and properties. Here, we apply process-induced strain by patterning shapes of a magnesium oxide (MgO_x) thin film on top of monolayer MoS_2, then quantify the relative contributions to strain and doping using Raman spectroscopy. We observe spatially varying strain profiles and build a traction−separation model to understand the mechanics at the 2D−substrate interface. We find that the monolayers undergo interfacial slip, which minimizes the strain transfer into the substrate and isolates larger strains in the monolayer, in contrast to conventional thin film mechanics, where strain transfer is dominated by out-of-plane shear. These models and strategies can be generalized to predict and design the strain in 2D materials induced during heterogeneous integration with arbitrary thin films. We demonstrate the utility of this approach by patterning the electronic structure of MoS_2 into complex shapes or engineering a heterostrain in the MoS_2/WSe_2 heterobilayer. These results demonstrate the design and control of strain in 2D monolayers and stacked heterobilayers with process-induced strain. We further show that the process-induced strain is predictable via theoretical and numerical models, which provide additional insights on understanding interface effects in the 2D strain transfer process. Together, these results offer a generalizable strategy to extract, predict, and design strain in emerging 2D systems induced during heterogeneous integration with nearly any process or thin film deposition.

RESULTS AND DISCUSSION

Quantifying Process-Induced Strain in 2D Monolayers. Figure 1 outlines how deposited stressors impact the strain and doping in the 2D materials. Figure 1a is a schematic cross-section of a patterned stressor deposited onto a monolayer of MoS_2 on a SiO_x/Si substrate. See Methods and Supporting Information Figure S1 for fabrication details. Briefly, we use gold-assisted large-area exfoliation[56] to generate large monolayer MoS_2 with lateral dimensions > 300 μm. We then use shadow masks or e-beam lithography to pattern squares (or other shapes, discussed later) with lateral sizes of 12−50 μm on top of the continuous MoS_2. We deposit a passivation layer of either Al_2O_x or HfO_x with a thickness of 5−6 nm, then use e-beam evaporation to deposit MgO_x with thicknesses of 0−60 nm. See Supporting Information Figure S2 for low-magnification images of the patterned arrays. We chose thin film MgO_x, because it is an established dielectric compressive stressor,[53,54] which is optically transparent and electrically insulating. While not strictly necessary, the passivation layers help both ensure good attachment of the stressor to the 2D surface and decouple the effects of strain and doping but must be accounted for as low stress layers in the mechanical modeling.

Shown in Supporting Information Figure S3 and Table S1, we use wafer-scale thin film stress testing to determine that the evaporated MgO_x has a built-in thickness-independent compressive stress of $\sigma_{film} = -0.95 \pm 0.09$ GPa. After deposition, the relaxation of the compressive stress in the MgO_x through expansion applies a thickness-dependent thin film force which transfers a tensile stress/strain to the underlying monolayer MoS_2.

Figure 1b shows the Raman spectra of monolayer MoS_2 with the characteristic E^1_{2g} and A_{1g} modes before (black) and after 30 nm MgO_x deposition (red), taken near the edge of a patterned, 50 μm wide square stressor (position indicated as the red dot in Figure 2a). After deposition, there is a redshift of 2.4 cm^{-1} of the E^1_{2g} mode and 3.2 cm^{-1} of the A_{1g} mode. Both Raman modes are sensitive to strain and doping, but shift at different rates, and so may be used as a nondestructive method to evaluate the strain and doping.[57] Figure 1c shows the scatter plots correlating the relative E^1_{2g} and A_{1g} peak positions before deposition (black) and after deposition of a 6 nm thick Al_2O_x passivation layer with no stressor (labeled 0 nm, yellow) and with increasing thicknesses of MgO_x of 15 nm (blue), 30 nm (red), and 60 nm (purple), all acquired from the same region near the edge of stressors. We also include an uncapped region far away (see the green dot in Figure 2a) from the patterned stressors after deposition (green). We correlate these relative shifts to previous studies to deduce the changes in strain and doping,[39,58] shown as tilted axes in Figure 1c (derivation in Supporting Information S1). The data show that the initial deposition of the Al_2O_x passivation layer induces a change in n-doping of $(0.61 \pm 0.07) \times 10^{13}$ cm^{-2}, but a minimal change in strain of 0.06 ± 0.03%. Moreover, the uncapped region shows a similar change in the doping and strain after deposition. We attribute the initial change in doping during the high-temperature e-beam deposition to both the thermal effects (far away)[59] and the creation of defects at the 2D/oxide interface.[60] Next, the addition of MgO_x on top of the

https://doi.org/10.1021/acsnano.3c09354
ACS Nano XXXX, XXX, XXX−XXX

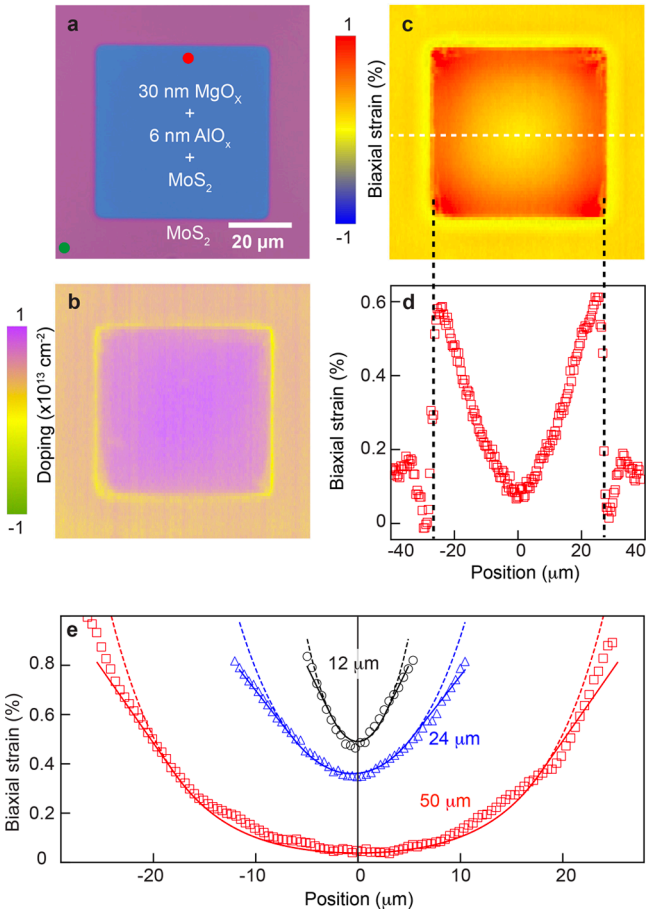

Figure 2. Spatially varying strain under patterned stressors. (a) Optical image of a 50 μm wide patterned square of a 30 nm thick MgO_x stressor on monolayer MoS_2 on a SiO_x/Si substrate. The red dot denotes the location where the data in Figure 1b,c are taken, and the green dot corresponds to the uncapped MoS_2 data in Figure 1c (green cluster). (b, c) Maps of extracted doping and biaxial strain in MoS_2 extracted from hyperspectral Raman mapping. (d) Biaxial strain of MoS_2 versus position corresponding with the white dashed line in (c). (e) The biaxial strain profile versus position along the center axis for square 30 nm thick stressors with widths of 12 μm (black), 24 μm (blue), and 50 μm (red). The shapes are the experimental data, the solid lines are fitted piecewise functions using the analytical model, and the dashed lines are fitted hyperbolic functions.

passivation layer induces tensile biaxial strain and only minimal additional changes in n-doping. Effectively, the use of the passivation layer is decoupling the impact of strain and doping during the deposition process. Moreover, changing the thickness of the stressor increases the tensile biaxial strain nearly linearly. We estimate an effective tensile biaxial strain of 0.58 ± 0.02% and doping density of (7.0 ± 0.6) × 10^{12} cm^{-2} near the edge of a 50 μm wide square with a 6 nm thick Al_2O_x and 30 nm thick MgO_x stressor. The increase in strain with an increase in stressor thickness is consistent with a linearly increasing thin film force. For simplicity, hereafter we will always refer to the effective biaxial strain simply as strain. As discussed in Supporting Information Section 2, this is a good approximation except right at the edges of stressors.

Interfacial Mechanics Determine Spatial Strain Profiles. Figure 2 investigates the spatial distribution of strain in MoS_2 both inside and outside a patterned stressor. Figure 2a shows an optical image of a shadow-mask-patterned square stressor 50 μm × 50 μm and 30 nm thick on continuous monolayer MoS_2. Figures 2b and 2c show the corresponding doping and strain in monolayer MoS_2. We extracted this local strain and doping using Raman hyperspectral imaging to form a two-dimensional map of Raman peak shifts and then performed the transformation shown in Figure 1c. Supporting Information Figures S4–S6 provide additional maps of peak parameters and extracted strain and doping, before and after deposition and as a function of laser polarization. The doping under the stressor seen in Figure 2b shows a spatially uniform shift of (4 ± 0.7) × 10^{12} cm^{-2}, compared with that of the surrounding region. In comparison, the strain under the stressor shows a complex profile following the shape of the stressor.

Figure 2d highlights these variations by plotting the strain line profile along the center of the square stressor (white dashed line in Figure 2c). The black dashed line marks the edge of the stressor. The strain reaches a minimum at the center of the stressor and increases when approaching the edges. At the edge, the strain undergoes an inversion with a small region of compressive strain that propagates outside the stressor. As a comparison, patterned stressors deposited on silicon also show complex size-dependent strain profiles and have been modeled as the local transfer of strain into the underlying substrate through combinations of 3D in-plane and out-of-plane shear and the boundary conditions set by the edges of the stressor.[50,51,61,62] As we will investigate, the vdW interface in the monolayer MoS_2–substrate leads to important differences in the resulting strain profile.

We further investigate the mechanics of the complex strain profile by measuring square stressors of size ranging from 12 to 50 μm. We made different sizes of stressors in the same sample by electron beam lithography (details in Methods). Figure 2e plots the resulting extracted strain versus position on the same scale through the center line of each square with zero position corresponding to the middle of each stressor. The points are experimentally measured strains. The data right at and outside the edges are intentionally cut off to focus on the changes inside the stressors. Supporting Information Figure S7 shows the corresponding strain map of the entire stressor array as well as a plot of the middle and edge stress versus size. Discussed further in the models below, there is a nontrivial evolution in the strain profile as a function of stressor size from pure hyperbolic behavior (dashed lines) to a piecewise solution with a hyperbolic profile near the center and linear profile near the edges (solid lines).

Shown schematically in Figure 3a,b, we propose a traction–separation model[63–65] to describe the interfacial mechanics of out-of-plane transfer of in-plane strain across the 2D–substrate interface and resulting in-plane strain profile within the monolayer. Figure 3a depicts a schematic of the square stressor model, where the stressor is smaller than the underlying 2D layer. As shown in Figure 3b, the interface moves from the mechanically bonded to the slip regime with increasing displacement δ. To relate this model to the measurements, the strain in the 2D layer is the derivative of the displacement $\varepsilon(x) = \frac{d\delta(x)}{dx}$. In the mechanically bonded regime, the in-plane displacement across the 2D–substrate interface δ and interfacial traction τ are linearly proportional, defined as $\tau = K_b\delta$, where K_b is the interfacial traction coefficient. Above the critical damage initiation threshold

https://doi.org/10.1021/acsnano.3c09354
ACS Nano XXXX, XXX, XXX–XXX

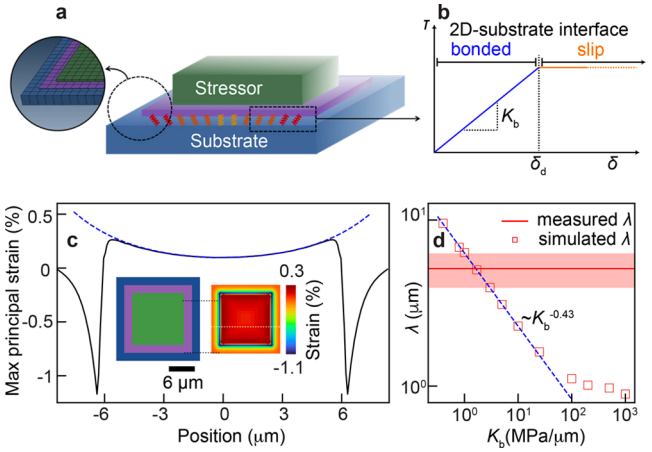

Figure 3. (a) Schematic representing the model for a 2D monolayer sandwiched between a stressor and a substrate, with a traction−separation model defining the behavior at the 2D−substrate interface. Circled graphic shows the finite element model mesh, with size and geometry not to scale. (b) Conceptual plot of defining the constituent relation between interfacial traction stress τ and interfacial displacement δ, showing the transition between bonded and slip regimes. (c) Simulated strain profile of MoS_2 across the centerline of a 12 μm wide stressor. Dashed blue lines show hyperbolic fitting to the FEA strain profile inside the stressor. (d) Fitted strain decay length for simulations of different K_b compared with experimentally measured strain decay lengths, with $K_t = 10^4$ MPa/μm, $\delta_d = 20$ nm. Dashed blue line is a power law fit showing a relation of $K_b^{-0.43}$ for $K_b \ll K_t$.

displacement δ_d, the interface debonds and enters the slip regime, where the layers will slide past each other, leading to a constant $\tau = \tau_d$ with increasing δ. Similar models have been shown to describe strain transfer in systems such as 2D flakes on strained or bent soft substrates,[66−68] on strained metal foils,[69] and near the edges of inflated microballoons[70] or artificially stacked 2D heterostructures.[71]

We adapt the traction−separation model to describe the out-of-plane transfer of in-plane strain into monolayer MoS_2 sandwiched between a stressor and the underlying substrate. We assume that across the top interface the monolayer is well bonded to the stressor, which is supported by experimental studies from e-beam evaporation[60] or atomic layer deposition.[60,72,73] In contrast, the bottom interface between the monolayer and the substrate is formed by transfer of the 2D material and thus will be governed by vdW interactions and the traction−separation relation. In the model, we use the stressor thickness, t_{film}, and thin film stress, σ_{film}, based on experimental measurements provided above. Other material parameters can be found in Supporting Information Table S2. We note that the Young's modulus of the passivation layers is similar to the modulus of the stressor, but has low built-in stress and smaller thickness. As a result, we have found that the system is well approximated mechanically by treating the thin film stack as a single material with a lower effective stress. Before tackling the more complex 2D geometry, we describe a one-dimensional analytical model of a stressor with finite-width L but infinite length to understand the underlying behavior. The model defines a differential equation relating the local strain in the 2D monolayer $\varepsilon(x)$ as a function of position x to the material properties and geometry. Supporting Information Section S1.2 provides the full derivation. The resulting equation is a piecewise function of the strain depending on whether the interface is bonded ($\delta \le \delta_d$) or slipping ($\delta > \delta_d$). Denoting the center of the stressor as the zero position, the model predicts that

$$\frac{d^2\delta}{dx^2} = \frac{d\varepsilon}{dx} = \begin{cases} -\dfrac{\delta_d}{\lambda^2} & \text{if } x \le -x_d \\ \dfrac{\delta_d \sinh(x/\lambda)}{\lambda^2 \sinh(x_d/\lambda)} & \text{if } -x_d \le x \le x_d \\ \dfrac{\delta_d}{\lambda^2} & \text{if } x \ge x_d \end{cases} \quad (1)$$

Here, $\pm x_d$ marks the left and right position where slip begins ($\delta(\pm x_d) = \pm\delta_d$). In the bonded regime, the model predicts strain decay with a characteristic strain decay length λ associated with K_b, defined as

$$\lambda = \sqrt{E_{film} t_{film} / K_b} \quad (2)$$

In the slip regime, above the damage initiation threshold δ_d, the model predicts a linear strain profile. Taken together, the full solution is a piecewise function with a hyperbolic strain profile in the middle of the stressor and possible linear strain profile at the edges, though the linear strain profile onset depends on the magnitude of the applied strain and the size of the stressor. We note that the model also predicts the regions of compressive strain outside of the edges of the stressors. See Supporting Information Section S1.2 for more discussion.

The analytical model explains the transition between the hyperbolic and linear regimes observed in the strain profiles of Figure 2e, produces a good fit to the data, and provides a framework to understand how the strain profile will change with thickness, film modulus, and interfacial traction. We use the fits to extract the average measurable parameters for the strain profiles across all sizes: strain decay length $\lambda = 5.5 \pm 1.2$ μm, linear slope $0.06 \pm 0.01\%$ strain/μm, and damage initiation threshold $\delta_d = 16 \pm 5$ nm. Shown in Supporting Information Figure S7, the primary sources of error arise from long length scale heterogeneity in the sample. Similar variability is observed in other studies of traction on 2D materials.[74,75] We attribute it to variations in initial strain and local traction arising from the transfer process, surface roughness, and cleanliness of the interface across different regions of the transferred material.

Next, we use finite element analysis (FEA) to fully capture the strain distribution of MoS_2 for stressors with complex geometries, quantitatively relate the experimentally measured strain profile to interfacial parameters, and extract the properties of each interface. The FEA mesh is shown in the inset of Figure 3a. Figure 3c plots the simulated maximum principal strain profile extracted from the centerline of a 14 μm wide MoS_2 monolayer capped by a 12 μm wide and 30 nm thick square stressor. We assume thin film stress $\sigma_{film} = -1.0$ GPa, $K_b = 1.3$ MPa/μm, top interface traction coefficient $K_t = 10^4$ MPa/μm, and $\delta_d = 20$ nm. Supporting Information Table S1 provides the remaining material parameters. We note that this model can be adapted to parametrically study the role of any parameter in the system, but we choose the values that most closely match our experimental data. The insets compare the top-down view of the simulation geometry and the corresponding strain distribution map. Supporting Information Section S1.3 and Figure S8 explore anisotropic strain in the simulation. The simulated strain profiles show hyperbolic

https://doi.org/10.1021/acsnano.3c09354
ACS Nano XXXX, XXX, XXX−XXX

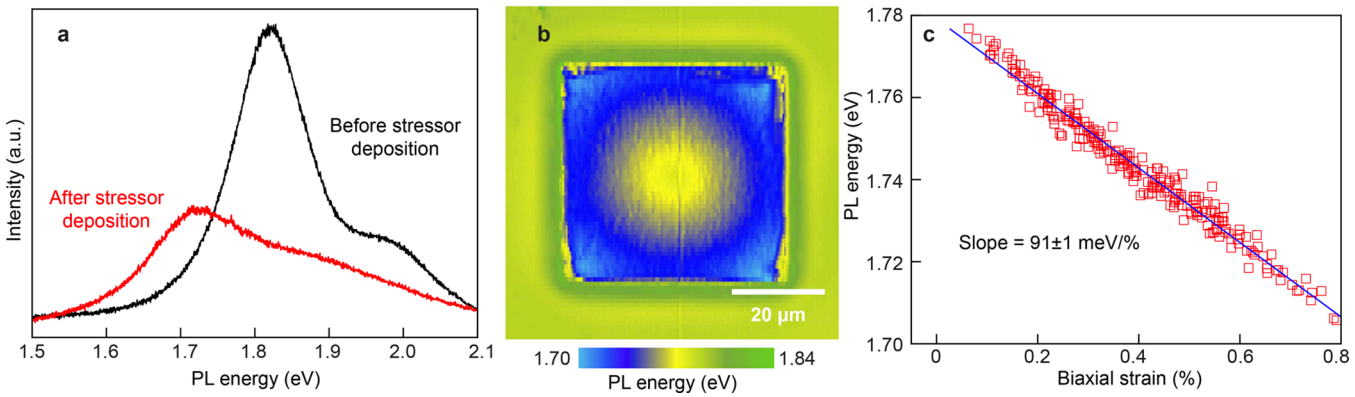

Figure 4. (a) Photoluminescence (PL) spectra of pristine MoS_2 (black) and MoS_2 capped by 30 nm of MgO_x (red), from the same sample and region shown in Figures 1 and 2. (b) Map of PL emission energy in monolayer MoS_2 capped with a square MgO_x stressor. (c) Scatter plot of PL transition energy vs strain in MgO_x-capped MoS_2. Blue line is a linear fit.

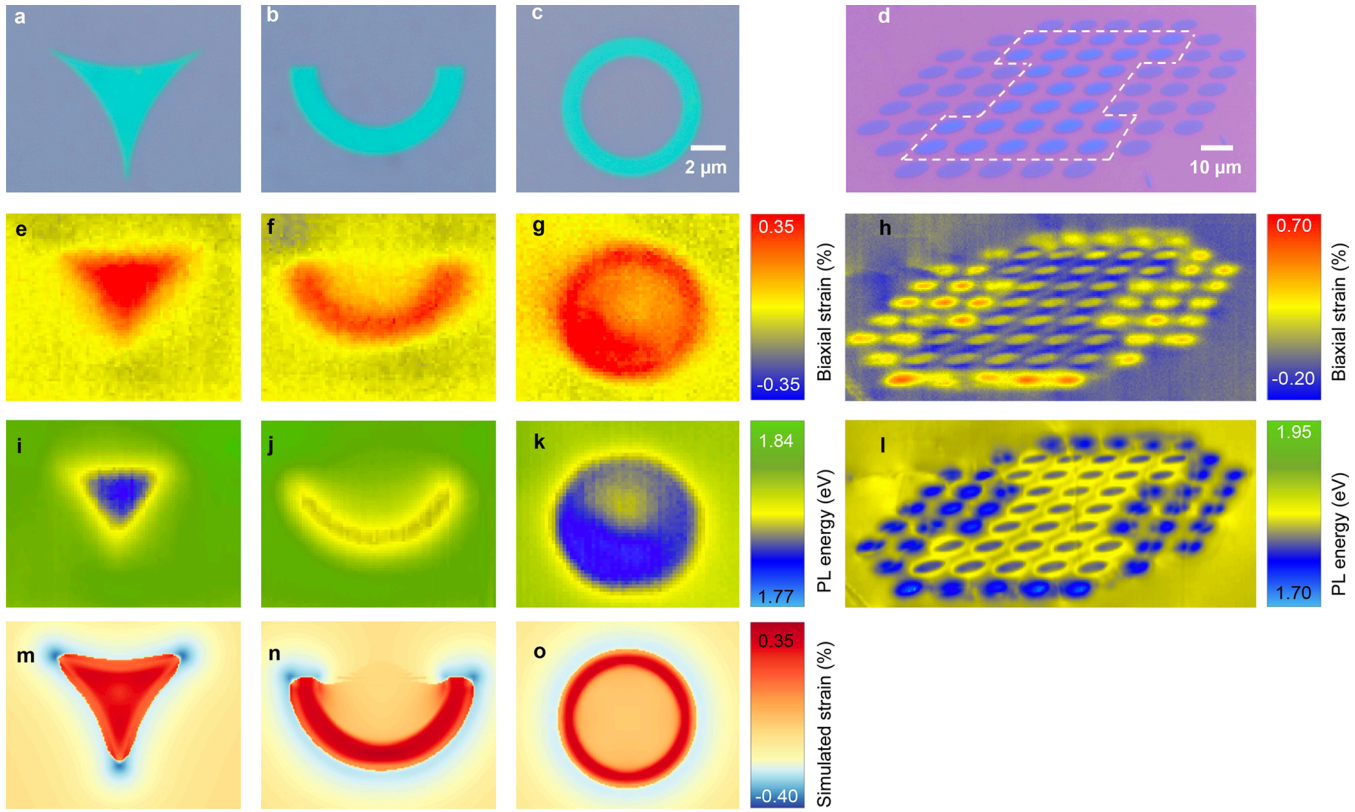

Figure 5. Designing strain profiles in 2D monolayer MoS_2. (a–d) Optical images of patterned stressors: (a) triangle, (b) half arc, (c) full ring, and (d) Illinois Material Science and Engineering Center (I-MRSEC) logo. (e–h) Corresponding maps of strain extracted from Raman spectroscopy. (i–l) Corresponding maps of the PL emission energy. (m–o) Corresponding simulated max principle strain profiles for the first 3 shapes from FEA.

behavior in the 2D material capped by the stressor, shown as a blue dashed line. This is in agreement with the measurements of the smallest stressor and consistent with the analytical model, although the exact magnitudes and onset of slip are sensitive to the chosen parameters. One difference is that the FEA model displays regions with larger compressive strain at the edges compared with spectroscopy measurements. We hypothesize that this difference could be explained by a combination of averaging effects rising from the diffraction-limited spatial resolution of the optical hyperspectral mapping of 0.7 μm or a different traction coefficient in the regions under versus outside the stressor.

FEA allows us to perform parametric analysis to explore the role of the key parameters affecting the strain profile, including geometric parameters (e.g., stressor thickness, size, shape, number of layers), material properties (e.g., Young's modulus, initial stress), and interfacial parameters (K_b, δ_d, K_t). In Figure 3d, the simulated hyperbolic strain decay length λ is plotted as a function of K_b, the interfacial traction coefficient of the bottom MoS_2–SiO_x interface on a log–log scale. There is a power law scaling between the parameters with a value of $K_b^{-0.43}$, which is in reasonable agreement with eq 2, which predicts a power law of $K_b^{-0.5}$. The pink line and band show the average and root-mean-square variations in the experimentally

https://doi.org/10.1021/acsnano.3c09354
ACS Nano XXXX, XXX, XXX–XXX

measured hyperbolic strain decay rates of 5.5 ± 1.2 MPa/μm, as extracted from Figure 2e. The crossover in the simulated and measured decay lengths corresponds to a K_b of 1.3 ± 0.7 MPa/μm. To compare, this value agrees with previous study on the graphene−SiO_x interface with an equivalent K_b of 0.82 MPa/μm[45,70] and 1 order of magnitude smaller than the graphene−polymer interface of 74 MPa/μm.[66] In Supporting Information Figure S9, we show an additional parametric analysis of the effect of different interfacial parameters on strain profiles. Together, the numerical and analytical models allow design and prediction of strain in 2D materials capped by a stressor in complex systems where experimental quantification is unachievable such as within device architectures and for structures below the optical diffraction limit.

Designing and Patterning Optical Properties with Strain. In the rest of the paper, we apply the developed techniques and models to explore applications at the forefront of 2D materials research, such as how to spatially pattern the electronic band structure and engineer layer-by-layer hetero-strain in 2D heterostructures.

Figure 4 explores how spatially varying strain modulates the local optical band gap in monolayer MoS_2 by performing a hyperspectral photoluminescence (PL) spectroscopy mapping. Figure 4a plots the PL intensity versus energy of MoS_2 before and after deposition near the edge of a stressor. After deposition, the PL emission energy shifts toward lower energy from 1.81 to 1.71 eV, and the peak emission intensity is reduced. Figure 4b is a map of the extracted PL emission energy on the same sample from Figure 2, allowing direct comparison. Inside the stressor, the spatial distribution of the emission energy closely follows that of the strain pattern, which allows us to cross-correlate the PL and strain maps. Figure 4c plots the resulting PL emission energy versus strain. We avoid the complexity from edge effects by cropping the data ~1 μm away from the edge to show the correlation only from inside the stressor. The PL emission energy tunes linearly with strain at a rate of 91 ± 1 meV/% strain.

In comparison, previous studies have shown that the PL transition energy is tunable via diverse techniques including applying uniaxial strain by bending 2D materials on a substrate[4,76] and biaxial strain by thermal expansion on a substrate[77] or via inflation of microballoons.[39] These studies, along with simulations,[78] find that strain tuning rates range from 44 to 72 meV/% for uniaxial strain and 99−112 meV/% for biaxial strains. Our measured values are similar to the range set by biaxial strains.

In Figure 5, we demonstrate designable strain profiles and optical properties by using lithography to pattern different shapes of stressors on monolayer MoS_2. The first row of Figures 5a−d shows the optical images of stressors patterned into a (a) triangle, (b) half arc, (c) full ring, and (d) Illinois Material Science and Engineering (I-MRSEC) logo. The second row, Figures 5e−h, maps the corresponding strain extracted from the Raman shifts. The third row, Figures 5i−l, maps the corresponding PL emission energy. The fourth row, Figures 5m−o, shows the simulated FEA principle strain maps. In each shape, the patterns defined in the stressors by lithography are transferred into the underlying MoS_2, which allows spatial definition of the local strain and optical band gap in the material, with an overall trend consistent with the simulation.

There are two interesting highlights in the strain maps. First, in the center of the ring in Figure 5c, both simulation and experiment show that the strain in the center region enclosed but uncovered by the stressor shows a residual tensile strain of 0.15%, showing that strain can be designed through the remote deposition and not just by depositing directly on top of the material. Second, in the MRSEC logo shown in 5d, we used two different depositions with different thicknesses to make the "I" (15 nm) stand out versus the surrounding (30 nm) and thus created two distinct strain levels in the same sample. This demonstrates that it is possible to spatially tailor the magnitude and not just shape of the strain profiles through repeated depositions. The ability to design the strain profile has diverse applications. For example, the asymmetric strain profiles made by patterning the triangles in Figure 5a have applications in directed exciton funneling. Taken together, these results demonstrate the versatility offered by patterning the process-induced strains for designing strain in 2D materials.

Interlayer Heterostrain in 2D Heterostructures. In Figure 6, we explore the application of stressors for heterostrain engineering in 2D heterostructures and the out-of-plane strain transfer across a 2D−2D interface. Figure 6a shows a schematic of a MoS_2−WSe_2 heterostructure on SiO_x/Si with patterned 30 nm thick MgO_x stressors deposited on top. We quantified the heterostrain between the constituent layers by fabricating two heterostructures with opposite stacking configurations: heterostructure-1 (HS-1) with MoS_2 top and WSe_2 bottom layer, and heterostructure-2 (HS-2) with WSe_2 top and MoS_2 bottom layer. The interlayer twist angles in the heterostructures are in a range of 17−27°, as established by optical images taken during transfer. As shown in Supporting Information Figure S10, the Raman transitions of

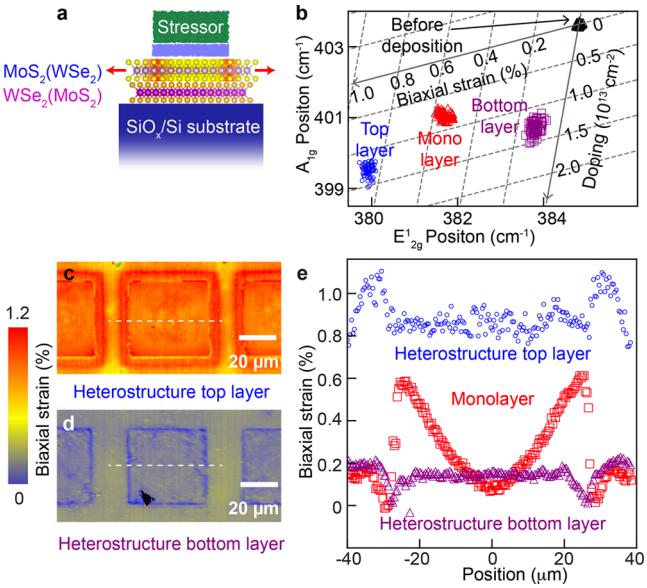

Figure 6. (a) Schematic of the cross-sectional view of a deposited square MgO_x stressor on a twisted MoS_2−WSe_2 (or, WSe_2−MoS_2) heterostructure. (b) Scatter plot of MoS_2 Raman E^1_{2g} and A_{1g} peak positions near the edge of a square 50 μm MgO_x stressor for MoS_2 monolayer (red) and for the heterostructure with MoS_2 on the top layer (blue) or bottom layer (purple). (c, d) Strain map of the heterostructure with MoS_2 as the (c) top and (d) bottom layer. (e) Corresponding cross-sectional strain profiles across the center line of 50 μm square stressors for a MoS_2 monolayer (red, from Figure 2d) and for the heterostructure with MoS_2 on the top layer (blue) or bottom layer (purple).

https://doi.org/10.1021/acsnano.3c09354
ACS Nano XXXX, XXX, XXX−XXX

the MoS_2, and WSe_2 are distinct, so we independently probe the peak shifts in each layer through a single spectroscopy measurement. We note that this ability to separate strain from each layer is important. In comparison, previous studies of process-induced strain were on multilayer MoS_2[53] where the signals from each layer are overlapping, making it impossible to discern strain layer-by-layer. We also note that unlike in MoS_2, the Raman transitions in WSe_2 overlap, making deconvolution of strain and doping effects more difficult.[79,80] Thus, we compare the Raman transitions in MoS_2 in the two different configurations to probe separately the strain in the top and bottom layers.

Figure 6b is a scatter plot comparing the Raman peak positions of the MoS_2 in four cases: monolayer before stressor deposition (black), monolayer after stressor deposition (red), heterostructure top layer (HS-1) after stressor deposition (blue), and heterostructure bottom layer (HS-2) after stressor deposition (purple), all taken from the same region near the edge of an identically sized 50 μm square stressor. The tilted axes quantify the biaxial strain and doping effects in MoS_2 from the relative peak positions. The doping induced is similar for all cases after deposition. Projecting along the strain axis, there are distinct strain magnitude differences in monolayer ($0.58 \pm 0.02\%$), bottom layer ($0.11 \pm 0.02\%$), and top layer ($0.86 \pm 0.04\%$) MoS_2.

Figure 6c and Figure 6d show the corresponding strain maps for the top MoS_2 layer in HS-1 and bottom MoS_2 layer in HS-2, respectively, while Figure 6e plots the strain through the center line of the maps, comparing the relative strain profile of the heterostructure top layer (blue), bottom layer (purple), and monolayer (red), from Figure 2. The maps show that the strain profile in the heterostructure under the stressor is more homogeneous compared with the monolayer. Additionally, for the top layer, there is a sharp rise in strain at the edge of the stressor, and the heightened strain extends significantly beyond the edge, to the point that patterned stressors separated by more than 25 μm have interacting strain profiles. The large heterostrain across the layers and the negligible strain in the bottom layer are consistent with the structural lubricity that arises in incommensurate twisted 2D vdW interfaces, which display friction orders of magnitude lower than conventional interfaces.[81]

Thus, we attribute the much higher strain in the top layer as resulting from the stressor applying the in-plane stress from the top down and a much lower onset of slip at the MoS_2/WSe_2 vdW interface compared with the underlying 2D−oxide interface. The homogeneity in the strain profile corroborates the FEA analysis from Figure 3d, which suggests that the low traction in the vdW interface will lead to a very long strain decay length compared with the size of the fabricated stressors. We note that the magnitude of the interlayer friction is well-known to depend on interlayer alignment,[81] so we hypothesize that aligned to low twist homo/heterostructures will show very different behavior. Finally, this same slow decay length will allow interaction between separated stressors, which partially explains the slow strain variations observed from underneath the stressors. That said, the fact that the strain rises between stressors rather than falls is surprising and does not follow from the models. Understanding the origin of these rises will require further modeling as well as analysis to deconvolve other effects not present in the monolayers like interlayer interactions which tune the Raman modes and interlayer nanoscale bubbles[9] and folds[82] resulting from transfer that lead to residual strain or slack.

These results demonstrate that process-induced strain engineering brings powerful capabilities to engineering moiré superlattices in 2D heterostructures. As a point of reference, there is a 0.2% mismatch in the lattice constant of MoS_2 (d = 0.322 nm) and WSe_2 (d = 0.329 nm). In comparison, the results above demonstrate that heterostrain engineering will modify the relative lattice constant by more than 0.8%. As a result, heterostrain engineering should strongly modify the wavelength of moiré superlattices at low twist angles in ways not accessible via twist alone, such as allowing lattice matching of mismatched heterostructures, bringing patternable and designable superlattices within a single structure and producing anisotropic superlattices from anisotropic heterostrain.

CONCLUSION

This work unites experiment and modeling to quantify strain transfer into 2D monolayers from integration with patterned thin film stressors and develop an understanding of the interfacial mechanics needed to predict and design the strain profiles. These capabilities provide a CMOS-compatible and scalable approach for patterning strain, with a drastic increase in the designability and control compared with current approaches, which we demonstrate with proof of concept applications to spatially pattern electronic structures of 2D semiconductors and pattern layer-by-layer heterostrain in 2D heterostructures. Moreover, while we focused on the combination of MoS_2 and MgO_x, our models and conclusions generalize to understanding and predicting strain in other vdW-bonded materials integrated with arbitrary thin films and other process technologies. Thus, this work serves as a foundation that is directly relevant to the design of highly strained nanosystems. A few specific examples to demonstrate the utility of this approach are as follows: (1) Exploring the size limits of patterned stressors and shape-induced gradients on 2D monolayers will enable methods for exciton confinement and funneling that cannot be achieved with the nanotemplating approaches currently used.[10,12] (2) Exploring how to design uniform strain profiles will have direct application to integration with nanoelectronics, such as the heterogeneous integration and strain-induced performance enhancement of 2D materials into semiconductor electronics.[6] (3) Exploring strain transfer in different combinations of 2D heterostructures or twisted bilayers will enable control over different dimensions of design for moiré engineering and strain-based superlattices.[55]

METHODS

Sample Fabrication. Supporting Information Figure S1 provides a graphical view of the fabrication flow which corresponds to steps i−iv below. (i) We start with synthetic MoS_2 and WSe_2 crystals (2D Semiconductors Inc.). To obtain monolayers, we use established recipes for gold-assisted layer-by-layer exfoliation of 2D materials.[56] We obtained the pristine, atomically clean gold surface by depositing 100 nm thick gold film onto polished silicon wafers (Nova Wafers Inc.) using electron-beam evaporation (Temescal Ebeam evaporator). (ii) We pattern a mask on top of the exfoliated 2D layers using either e-beam or shadow mask lithography. (iii) We deposit a thin layer of either 6 nm Al_2O_x with e-beam evaporation (sourced from Kurt J. Lesker Company, part number EVMALO1-3MMT) or 5 nm HfO_x with atomic layer deposition (ALD) (Cambridge NanoTech Savannah S100, 50 cycles) to promote the adhesion of the stressor to the 2D material and act as a passivation layer for decoupling strain

https://doi.org/10.1021/acsnano.3c09354
ACS Nano XXXX, XXX, XXX−XXX

and doping from deposition. We then use electron-beam evaporation to deposit MgO_x (Kurt J. Lesker Company, part number EVMMGO3-6MMT) of thicknesses ranging from 15 to 60 nm. During the deposition, we maintained a deposition rate of 0.5 Å per second. (iv) We removed the mask. In the case of electron-beam lithography, we lift off the mask with an acetone/IPA rinse. In the case of the shadow mask, we peel off the mask and obtain the sample. Samples discussed in Figure 1, Figure 2a to d, Figure 4, and Figure 6 are patterned by using a metal TEM grid (Ted Pella Inc.) as shadow mask and have 6 nm evaporated Al_2O_x as a passivation layer. Samples in Figure 2e and Figure 5 are patterned by 100 kV electron beam lithography (Raith EBPG 5150) with poly(methyl methacrylate) (PMMA) masks and have 5 nm ALD-grown HfO_x as a passivation layer.

Measuring the Thin Film Stress. We extracted the thin film stress using a variable-temperature film stress measurement system, FSM 500TC, which acts as a laser profilometer. We measure the curvature of a 4 in. 285 nm/550 μm SiO_x/Si wafer (Nova wafers) before and after depositing uniform, unpatterned films of MgO_x with thicknesses ranging from 20 to 80 nm. We then use Stoney's formula[83] to measure the film stress. Supporting Information Table S1 summarizes the results, and Supporting Information Figure S3 shows example curvature data. The built-in thin film stress for evaporated MgO_x is -0.95 ± 0.09 GPa.

Raman and PL Spectroscopy. For single-point Raman and PL spectroscopy measurements, we use a Renishaw confocal Raman microscope with a 532 nm laser, 2400 lines per mm gratings, and a filter of 0.1%. The power is kept below 100 μW, the integration time is kept below 10 s, and the laser spot size is estimated to be 1 μm. We perform the hyper-spectral Raman and PL spectroscopy with a Nanophoton 11 confocal Raman system with a 520 nm laser source under 100× magnification, where the spatial resolution is 0.7 μm, the scan power is kept below 0.7 mW per line, and the scan step size is 0.2 μm.

Finite Element Analysis Model. We used the commercial FEA package ABAQUS Standard solver. Material properties are summarized in Supporting Information Table S2. Unless otherwise explicitly stated, all simulations are for a 12 μm wide square stressor of thickness 30 nm. In this model, the mesh size is largely determined by the thinnest material thickness, which is 0.001 μm for MoS_2. Elements with high aspect ratios are undesirable because of the low accuracy of the solution due to the nodes of the element being far apart from each other. We used hexahedral 3D elements with a mesh size of 0.08 μm. The built-in stress of MgO_x is defined as a predefined stress field of −1.0 GPa. The bottom nodes of the SiO_x are constrained against all degrees of freedom, i.e., displacement and rotation. The interfacial properties are modeled as surface-to-surface interaction between the MgO_x-bottom/MoS_2-top and MoS_2-bottom/SiO_x-top surfaces using cohesive behavior with specified damage evolution properties. Here, the interfacial traction coefficients, K_t and K_b, and damage initiation threshold, δ_d, are defined. The simulations in the text use a K_t of 10^4 or 10^5 MPa/μm and K_b values ranging from 0.8 to 1000 MPa/μm, while ensuring that $K_t \gg K_b$. δ_d values in simulation range from 2 to 40 nm. Small sliding capability is included to enable the contacting surfaces to undergo small sliding relative to each other. For simulations shown in Figure 5, the top of the HfO_x and bottom of the MgO_x nodes are tied together to prevent any slip.

ASSOCIATED CONTENT

Data Availability Statement

The data that support the findings of this study, as well as the input files for the finite element simulations, are openly available in "Dataset for Design and Pattern Strain in 2D materials" at Illinois Data Bank, reference number 10.13012/B2IDB-2595358_V1.

Supporting Information

The Supporting Information is available free of charge at https://pubs.acs.org/doi/10.1021/acsnano.3c09354.

Derivation of the mechanical model of stressor-capped monolayer MoS_2, the optical detection of strain and doping of MoS_2 via Raman spectroscopy, the strain anisotropy and FEA settings, Supporting Figures S1−S10, Supporting Table S1 (PDF)

AUTHOR INFORMATION

Corresponding Author

Arend M. van der Zande − *Department of Mechanical Science and Engineering, University of Illinois Urbana−Champaign, Urbana, Illinois 61801, United States; Materials Research Laboratory, Department of Materials Science and Engineering, and Holonyak Micro and Nano Technology Lab, University of Illinois Urbana−Champaign, Urbana, Illinois 61801, United States;* orcid.org/0000-0001-5104-9646; Email: arendv@illinois.edu

Authors

Yue Zhang − *Department of Mechanical Science and Engineering, University of Illinois Urbana−Champaign, Urbana, Illinois 61801, United States;* orcid.org/0000-0002-3087-6965

M. Abir Hossain − *Department of Mechanical Science and Engineering, University of Illinois Urbana−Champaign, Urbana, Illinois 61801, United States; Center for Nanoscale Materials, Argonne National Laboratory, Lemont, Illinois 60439, United States;* orcid.org/0000-0003-1606-5960

Kelly J. Hwang − *Department of Mechanical Science and Engineering, University of Illinois Urbana−Champaign, Urbana, Illinois 61801, United States*

Paolo F. Ferrari − *Department of Mechanical Science and Engineering, University of Illinois Urbana−Champaign, Urbana, Illinois 61801, United States;* orcid.org/0000-0001-9787-553X

Joseph Maduzia − *Department of Mechanical Science and Engineering, University of Illinois Urbana−Champaign, Urbana, Illinois 61801, United States*

Tara Peña − *Department of Electrical and Computer Engineering, University of Rochester, Rochester, New York 14627, United States*

Stephen M. Wu − *Department of Electrical and Computer Engineering, University of Rochester, Rochester, New York 14627, United States;* orcid.org/0000-0001-6079-3354

Elif Ertekin − *Department of Mechanical Science and Engineering, University of Illinois Urbana−Champaign, Urbana, Illinois 61801, United States; Materials Research Laboratory, University of Illinois Urbana−Champaign, Urbana, Illinois 61801, United States;* orcid.org/0000-0002-7816-1803

Complete contact information is available at: https://pubs.acs.org/10.1021/acsnano.3c09354

Author Contributions

▽Y.Z., M.A.H., and K.J.H. contributed equally to this work. A.M.v.d.Z, Y.Z, and M.A.H. conceived the concept for the study. Under A.M.v.d.Z.'s supervision, Y.Z. and M.A.H. performed monolayer sample fabrication, spectroscopy measurements, and analysis to extract local strains. M.A.H. performed heterostructure fabrication, spectroscopy measurements, and analysis of heterostrain. P.F.F. assisted in sample fabrication. J.M. assisted in thin film stressor deposition. T.P. and S.M.W. provided crucial guidance on the process

https://doi.org/10.1021/acsnano.3c09354
ACS Nano XXXX, XXX, XXX−XXX

parameters and materials needed for stressor deposition and film stress analysis. Under A.M.v.d.Z.'s supervision, Y.Z. and K.J.H. developed the mechanics models. Under A.M.v.d.Z.'s and E.E.'s supervision, K.J.H. built the finite element analysis simulations. All authors read and contributed to the manuscript.

Notes

The authors declare no competing financial interest.

ACKNOWLEDGMENTS

This work was primarily supported by an NSF-MRSEC under Award Number DMR-2309037, with partial support from NSF-CAREER Award Number CMMI-184673. K.J.H. acknowledges support from the Digimat Graduate Fellowship, supported by the National Science Foundation under Grant No. 1922758. T.P. and S.W. acknowledge support by NSF OMA-1936250 and NSF ECCS-1942815. T.P. acknowledges support from NSF GRFP DGE-1939268. This work was carried out in part in the Holonyak Micro and Nano Technology Laboratory, the Materials Research Laboratory Central Facilities (MRL), and the Micro and Nano Mechanical Systems Clean Room (MNMS), all at the University of Illinois. The authors acknowledge the use of facilities and instrumentation supported by NSF through the University of Illinois Materials Research Science and Engineering Center DMR-2309037. Computational resources were provided by the Visualization Lab at the Beckman Institute for Advanced Science and Technology. The authors also acknowledge helpful discussions with Pinshane Huang and Harley Johnson.

REFERENCES

(1) Yu, J.; Hossain, M. A.; Kim, S.; Ferrari, P. F.; Huang, S.; Zhang, Y.; Kim, H.; Michel, D. A.; van der Zande, A. M. Mechanically sensing and tailoring electronic properties in two-dimensional atomic membranes. *Curr. Opin. Solid State Mater. Sci.* **2021**, *25*, 100900.

(2) Lemme, M. C.; Akinwande, D.; Huyghebaert, C.; Stampfer, C. 2D materials for future heterogeneous electronics. *Nat. Commun.* **2022**, *13*, 1392.

(3) Huyghebaert, C.; et al. 2D materials: roadmap to CMOS integration. *2018 IEEE Int. Electron Devices Meet. (IEDM).* **2018**, 22−1.

(4) Conley, H. J.; Wang, B.; Ziegler, J. I.; Haglund Jr, R. F.; Pantelides, S. T.; Bolotin, K. I. Bandgap engineering of strained monolayer and bilayer MoS2. *Nano Lett.* **2013**, *13*, 3626−3630.

(5) Dhakal, K. P.; Roy, S.; Jang, H.; Chen, X.; Yun, W. S.; Kim, H.; Lee, J.; Kim, J.; Ahn, J.-H. Local strain induced band gap modulation and photoluminescence enhancement of multilayer transition metal dichalcogenides. *Chem. Mater.* **2017**, *29*, 5124−5133.

(6) Datye, I. M.; Daus, A.; Grady, R. W.; Brenner, K.; Vaziri, S.; Pop, E. Strain-Enhanced Mobility of Monolayer MoS2. *Nano Lett.* **2022**, *22*, 8052−8059.

(7) Feng, J.; Qian, X.; Huang, C.-W.; Li, J. Strain-engineered artificial atom as a broad-spectrum solar energy funnel. *Nat. Photonics* **2012**, *6*, 866−872.

(8) Moon, H.; Grosso, G.; Chakraborty, C.; Peng, C.; Taniguchi, T.; Watanabe, K.; Englund, D. Dynamic exciton funneling by local strain control in a monolayer semiconductor. *Nano Lett.* **2020**, *20*, 6791−6797.

(9) Darlington, T.; et al. Imaging strain-localized excitons in nanoscale bubbles of monolayer WSe2 at room temperature. *Nat. Nanotechnol* **2020**, *15*, 854−860.

(10) Dirnberger, F.; Ziegler, J. D.; Faria Junior, P. E.; Bushati, R.; Taniguchi, T.; Watanabe, K.; Fabian, J.; Bougeard, D.; Chernikov, A.; Menon, V. M. Quasi-1D exciton channels in strain-engineered 2D materials. *Sci. Adv.* **2021**, *7*, eabj3066.

(11) Bai, Y.; Zhou, L.; Wang, J.; Wu, W.; McGilly, L. J.; Halbertal, D.; Lo, C. F. B.; Liu, F.; Ardelean, J.; Rivera, P.; et al. Excitons in strain-induced one-dimensional moiré potentials at transition metal dichalcogenide heterojunctions. *Nat. Mater.* **2020**, *19*, 1068−1073.

(12) Harats, M. G.; Kirchhof, J. N.; Qiao, M.; Greben, K.; Bolotin, K. I. Dynamics and efficient conversion of excitons to trions in non-uniformly strained monolayer WS2. *Nat. Photonics* **2020**, *14*, 324−329.

(13) Qiao, J.-B.; Yin, L.-J.; He, L. Twisted graphene bilayer around the first magic angle engineered by heterostrain. *Phys. Rev. B* **2018**, *98*, 235402.

(14) Kazmierczak, N. P.; Van Winkle, M.; Ophus, C.; Bustillo, K. C.; Carr, S.; Brown, H. G.; Ciston, J.; Taniguchi, T.; Watanabe, K.; Bediako, D. K. Strain fields in twisted bilayer graphene. *Nat. Mater.* **2021**, *20*, 956−963.

(15) So, J.-P.; Jeong, K.-Y.; Lee, J. M.; Kim, K.-H.; Lee, S.-J.; Huh, W.; Kim, H.-R.; Choi, J.-H.; Kim, J. M.; Kim, Y. S.; Lee, C.-H.; Nam, S.; Park, H.-G. Polarization control of deterministic single-photon emitters in monolayer WSe2. *Nano Lett.* **2021**, *21*, 1546−1554.

(16) Palacios-Berraquero, C.; Kara, D. M.; Montblanch, A. R.-P.; Barbone, M.; Latawiec, P.; Yoon, D.; Ott, A. K.; Loncar, M.; Ferrari, A. C.; Atatüre, M. Large-scale quantum-emitter arrays in atomically thin semiconductors. *Nat. Commun.* **2017**, *8*, 15093.

(17) Grosso, G.; Moon, H.; Lienhard, B.; Ali, S.; Efetov, D. K.; Furchi, M. M.; Jarillo-Herrero, P.; Ford, M. J.; Aharonovich, I.; Englund, D. Tunable and high-purity room temperature single-photon emission from atomic defects in hexagonal boron nitride. *Nat. Commun.* **2017**, *8*, 1−8.

(18) Kern, J.; Niehues, I.; Tonndorf, P.; Schmidt, R.; Wigger, D.; Schneider, R.; Stiehm, T.; Michaelis de Vasconcellos, S.; Reiter, D. E.; Kuhn, T.; Bratschitsch, R. Nanoscale positioning of single-photon emitters in atomically thin Wse2. *Adv. Mater.* **2016**, *28*, 7101−7105.

(19) Mukherjee, A.; Chakraborty, C.; Qiu, L.; Vamivakas, A. N. Electric field tuning of strain-induced quantum emitters in WSe2. *AIP Adv.* **2020**, *10*, 075310.

(20) Duerloo, K.-A. N.; Li, Y.; Reed, E. J. Structural phase transitions in two-dimensional Mo-and W-dichalcogenide monolayers. *Nat. Commun.* **2014**, *5*, 4214.

(21) Song, S.; Keum, D. H.; Cho, S.; Perello, D.; Kim, Y.; Lee, Y. H. Room temperature semiconductor−metal transition of MoTe2 thin films engineered by strain. *Nano Lett.* **2016**, *16*, 188−193.

(22) Hou, W.; Azizimanesh, A.; Sewaket, A.; Peña, T.; Watson, C.; Liu, M.; Askari, H.; Wu, S. M. Strain-based room-temperature non-volatile MoTe2 ferroelectric phase change transistor. *Nat. Nanotechnol.* **2019**, *14*, 668−673.

(23) Levy, N.; Burke, S. A.; Meaker, K. L.; Panlasigui, M.; Zettl, A.; Guinea, F.; Neto, A. H. C.; Crommie, M. F. Strain-Induced PseudoMagnetic Fields Greater Than 300 T in Graphene Nanobubbles. *Science* **2010**, *329*, 544−547.

(24) Hsu, C.-C.; Teague, M.; Wang, J.-Q.; Yeh, N.-C. Nanoscale strain engineering of giant pseudo-magnetic fields, valley polarization, and topological channels in graphene. *Sci. Adv.* **2020**, *6*, 9488.

(25) Jiang, Y.; Mao, J.; Duan, J.; Lai, X.; Watanabe, K.; Taniguchi, T.; Andrei, E. Y. Visualizing strain-induced pseudomagnetic fields in graphene through an hBN magnifying glass. *Nano Lett.* **2017**, *17*, 2839−2843.

(26) Zhang, Y.; Kim, Y.; Gilbert, M. J.; Mason, N. Magnetotransport in a strain superlattice of graphene. *Appl. Phys. Lett.* **2019**, *115*, 143508.

(27) Ma, Y.; Dai, Y.; Guo, M.; Niu, C.; Zhu, Y.; Huang, B. Evidence of the existence of magnetism in pristine VX2 monolayers (X= S, Se) and their strain-induced tunable magnetic properties. *ACS Nano* **2012**, *6*, 1695−1701.

(28) Vsivkins, M.; Kurdi, S.; Lee, M.; Slotboom, B. J.; Xing, W.; Manas-Valero, S.; Coronado, E.; Jia, S.; Han, W.; van der Sar, T.; van der Zant, H.; Steeneken, P. Nanomechanical probing and strain tuning of the Curie temperature in suspended Cr2Ge2Te6-based heterostructures. *npj 2D Mater. Appl.* **2022**, *6*, 41.

https://doi.org/10.1021/acsnano.3c09354
ACS Nano XXXX, XXX, XXX−XXX

(29) Lee, J.; Wang, Z.; Xie, H.; Mak, K. F.; Shan, J. Valley magnetoelectricity in single-layer MoS2. *Nat. Mater.* **2017**, *16*, 887−891.
(30) Bertolazzi, S.; Brivio, J.; Kis, A. Stretching and breaking of ultrathin MoS2. *ACS Nano* **2011**, *5*, 9703−9709.
(31) Alden, J. S.; Tsen, A. W.; Huang, P. Y.; Hovden, R.; Brown, L.; Park, J.; Muller, D. A.; McEuen, P. L. Strain solitons and topological defects in bilayer graphene. *Proc. Natl. Acad. Sci.* **2013**, *110*, 11256−11260.
(32) Koren, E.; Lörtscher, E.; Rawlings, C.; Knoll, A. W.; Duerig, U. Adhesion and friction in mesoscopic graphite contacts. *Science* **2015**, *348*, 679−683.
(33) Han, E.; Yu, J.; Annevelink, E.; Son, J.; Kang, D. A.; Watanabe, K.; Taniguchi, T.; Ertekin, E.; Huang, P. Y.; van der Zande, A. M. Ultrasoft slip-mediated bending in few-layer graphene. *Nat. Mater.* **2020**, *19*, 305−309.
(34) Lee, G.-H.; Cooper, R. C.; An, S. J.; Lee, S.; van der Zande, A.; Petrone, N.; Hammerberg, A. G.; Lee, C.; Crawford, B.; Oliver, W.; Kysar, J. W.; Hone, J. High-strength chemical-vapor−deposited graphene and grain boundaries. *Science* **2013**, *340*, 1073−1076.
(35) Castellanos-Gomez, A.; Singh, V.; van der Zant, H. S.; Steele, G. A. Mechanics of freely-suspended ultrathin layered materials. *Ann. Phys.* **2015**, *527*, 27−44.
(36) Li, H.; Contryman, A. W.; Qian, X.; Ardakani, S. M.; Gong, Y.; Wang, X.; Weisse, J. M.; Lee, C. H.; Zhao, J.; Ajayan, P. M.; Li, J.; Manoharan, H.; Zheng, X. Optoelectronic crystal of artificial atoms in strain-textured molybdenum disulphide. *Nat. Commun.* **2015**, *6*, 7381.
(37) Zhang, Y.; Heiranian, M.; Janicek, B.; Budrikis, Z.; Zapperi, S.; Huang, P. Y.; Johnson, H. T.; Aluru, N. R.; Lyding, J. W.; Mason, N. Strain modulation of graphene by nanoscale substrate curvatures: a molecular view. *Nano Lett.* **2018**, *18*, 2098−2104.
(38) Bunch, J. S.; Verbridge, S. S.; Alden, J. S.; Van Der Zande, A. M.; Parpia, J. M.; Craighead, H. G.; McEuen, P. L. Impermeable atomic membranes from graphene sheets. *Nano Lett.* **2008**, *8*, 2458−2462.
(39) Lloyd, D.; Liu, X.; Christopher, J. W.; Cantley, L.; Wadehra, A.; Kim, B. L.; Goldberg, B. B.; Swan, A. K.; Bunch, J. S. Band gap engineering with ultralarge biaxial strains in suspended monolayer MoS2. *Nano Lett.* **2016**, *16*, 5836−5841.
(40) Shepard, G. D.; Ajayi, O. A.; Li, X.; Zhu, X.; Hone, J.; Strauf, S. Nanobubble induced formation of quantum emitters in monolayer semiconductors. *2D Mater.* **2017**, *4*, 021019.
(41) Thai, K. Y.; Park, I.; Kim, B. J.; Hoang, A. T.; Na, Y.; Park, C. U.; Chae, Y.; Ahn, J.-H. MoS2/graphene photodetector array with strain-modulated photoresponse up to the near-infrared regime. *ACS Nano* **2021**, *15*, 12836−12846.
(42) Castellanos-Gomez, A.; Roldán, R.; Cappelluti, E.; Buscema, M.; Guinea, F.; van der Zant, H. S.; Steele, G. A. Local strain engineering in atomically thin MoS2. *Nano Lett.* **2013**, *13*, 5361−5366.
(43) Deng, S.; Berry, V. Wrinkled, rippled and crumpled graphene: an overview of formation mechanism, electronic properties, and applications. *Mater. Today* **2016**, *19*, 197−212.
(44) Chen, W.; Gui, X.; Yang, L.; Zhu, H.; Tang, Z. Wrinkling of two-dimensional materials: Methods, properties and applications. *Nanoscale Horiz.* **2019**, *4*, 291−320.
(45) Yu, J.; Kim, S.; Ertekin, E.; Van Der Zande, A. M. Material-dependent evolution of mechanical folding instabilities in two-dimensional atomic membranes. *ACS Appl. Mater. Interfaces* **2020**, *12*, 10801−10808.
(46) Lee, J.; Yun, S. J.; Seo, C.; Cho, K.; Kim, T. S.; An, G. H.; Kang, K.; Lee, H. S.; Kim, J. Switchable, tunable, and directable exciton funneling in periodically wrinkled WS2. *Nano Lett.* **2021**, *21*, 43−50.
(47) Thompson, S.; et al. A 90-nm logic technology featuring strained-silicon. *IEEE Trans. Electron Devices* **2004**, *51*, 1790−1797.
(48) Welser, J. NMOS and PMOS transistors fabricated in strain silicon/relaxed silicon-germanium structures. *Technol. Dig. - Int. Electron Devices Meet.* **1992**.
(49) Welser, J.; Hoyt, J.; Gibbons, J. Electron mobility enhancement in strained-Si n-type metal-oxide-semiconductor field-effect transistors. *IEEE Electron Device Lett.* **1994**, *15*, 100−102.
(50) Jain, S.; Harker, A.; Atkinson, A.; Pinardi, K. Edge-induced stress and strain in stripe films and substrates: A two-dimensional finite element calculation. *J. Appl. Phys.* **1995**, *78*, 1630−1637.
(51) Pinardi, K.; Jain, S.; Willander, M.; Atkinson, A.; Maes, H.; Van Overstraeten, R. A method to interpret micro-Raman experiments made to measure nonuniform stresses: Application to local oxidation of silicon structures. *J. Appl. Phys.* **1998**, *84*, 2507−2512.
(52) Krzeminski, C. D. Stress mapping in strain-engineered silicon p-type MOSFET device: A comparison between process simulation and experiments. *J. Vac. Sci. Technol., B: Nanotechnol. Microelectron.: Mater., Process., Meas., Phenom.* **2012**, *30*, 022203.
(53) Peña, T.; Chowdhury, S. A.; Azizimanesh, A.; Sewaket, A.; Askari, H.; Wu, S. M. Strain engineering 2D MoS2 with thin film stress capping layers. *2D Mater.* **2021**, *8*, 045001.
(54) Azizimanesh, A.; Peña, T.; Sewaket, A.; Hou, W.; Wu, S. M. Uniaxial and biaxial strain engineering in 2D MoS2 with lithographically patterned thin film stressors. *Appl. Phys. Lett.* **2021**, *118*, 213104.
(55) Peña, T.; Dey, A.; Chowdhury, S. A.; Azizimanesh, A.; Hou, W.; Sewaket, A.; Watson, C.; Askari, H.; Wu, S. M. Moiré engineering in 2D heterostructures with process-induced strain. *Appl. Phys. Lett.* **2023**, *122*, 143101.
(56) Liu, F.; Wu, W.; Bai, Y.; Chae, S. H.; Li, Q.; Wang, J.; Hone, J.; Zhu, X.-Y. Disassembling 2D van der Waals crystals into macroscopic monolayers and reassembling into artificial lattices. *Science* **2020**, *367*, 903−906.
(57) Yang, L.; Cui, X.; Zhang, J.; Wang, K.; Shen, M.; Zeng, S.; Dayeh, S. A.; Feng, L.; Xiang, B. Lattice strain effects on the optical properties of MoS2 nanosheets. *Sci. Rep.* **2014**, *4*, 5649.
(58) Michail, A.; Delikoukos, N.; Parthenios, J.; Galiotis, C.; Papagelis, K. Optical detection of strain and doping inhomogeneities in single layer MoS2. *Appl. Phys. Lett.* **2016**, *108*, 173102.
(59) Valsaraj, A.; Chang, J.; Rai, A.; Register, L. F.; Banerjee, S. K. Theoretical and experimental investigation of vacancy-based doping of monolayer MoS2 on oxide. *2D Mater.* **2015**, *2*, 045009.
(60) Liu, Y.; Guo, J.; Zhu, E.; Liao, L.; Lee, S.-J.; Ding, M.; Shakir, I.; Gambin, V.; Huang, Y.; Duan, X. Approaching the Schottky−Mott limit in van der Waals metal−semiconductor junctions. *Nature* **2018**, *557*, 696−700.
(61) Suhir, E. Stresses in multilayered thin films on a thick substrate. *MRS Online Proc. Libr. (OPL)* **1987**, *91*, 73.
(62) Fischer, A.; Richter, H. Elastic stress relaxation in SiGe epilayers on patterned Si substrates. *J. Appl. Phys.* **1994**, *75*, 657−659.
(63) Cox, H. The elasticity and strength of paper and other fibrous materials. *Br. J. Appl. Phys.* **1952**, *3*, 72.
(64) Kelly, A.; Macmillan, N. *Strong Solids*, 3rd ed.; Monographs on the Physics and Chem. Mater.; Clarendon Press: Oxford, 1986; Vol. 9; pp 395−456.
(65) Jiang, T.; Huang, R.; Zhu, Y. Interfacial sliding and buckling of monolayer graphene on a stretchable substrate. *Adv. Funct. Mater.* **2014**, *24*, 396−402.
(66) Guo, G.; Zhu, Y. Cohesive-shear-lag modeling of interfacial stress transfer between a monolayer graphene and a polymer substrate. *J. Appl. Mech.* **2015**, *82*, 031005.
(67) Gong, L.; Kinloch, I. A.; Young, R. J.; Riaz, I.; Jalil, R.; Novoselov, K. S. Interfacial stress transfer in a graphene monolayer nanocomposite. *Adv. Mater.* **2010**, *22*, 2694−2697.
(68) Young, R. J.; Gong, L.; Kinloch, I. A.; Riaz, I.; Jalil, R.; Novoselov, K. S. Strain mapping in a graphene monolayer nanocomposite. *ACS Nano* **2011**, *5*, 3079−3084.
(69) Bronsgeest, M. S.; Bendiab, N.; Mathur, S.; Kimouche, A.; Johnson, H. T.; Coraux, J.; Pochet, P. Strain relaxation in CVD graphene: wrinkling with shear lag. *Nano Lett.* **2015**, *15*, 5098−5104.
(70) Wang, G.; Dai, Z.; Wang, Y.; Tan, P.; Liu, L.; Xu, Z.; Wei, Y.; Huang, R.; Zhang, Z. Measuring interlayer shear stress in bilayer graphene. *Phys. Rev. Lett.* **2017**, *119*, 036101.

https://doi.org/10.1021/acsnano.3c09354
ACS Nano XXXX, XXX, XXX−XXX

(71) Kumar, H.; Dong, L.; Shenoy, V. B. Limits of coherency and strain transfer in flexible 2D van der Waals heterostructures: formation of strain solitons and interlayer debonding. *Sci. Rep.* **2016**, *6*, 21516.
(72) Kilpi, L.; Ylivaara, O. M.; Vaajoki, A.; Malm, J.; Sintonen, S.; Tuominen, M.; Puurunen, R. L.; Ronkainen, H. Microscratch testing method for systematic evaluation of the adhesion of atomic layer deposited thin films on silicon. *J. Vac. Sci. Technol., A* **2016**, *34*, 01A124.
(73) Hossain, M. A.; Zhang, Y.; Van Der Zande, A. M. Strain engineering photonic properties in monolayer semiconductors through mechanically-reconfigurable wrinkling. *Physical Chemistry of Semiconductor Materials and Interfaces XIX* **2020**, 1146404.
(74) Wang, G.; Dai, Z.; Wang, Y.; Tan, P.; Liu, L.; Xu, Z.; Wei, Y.; Huang, R.; Zhang, Z. Measuring Interlayer Shear Stress in Bilayer Graphene. *Phys. Rev. Lett.* **2017**, *119*, 036101.
(75) Kitt, A. L.; Qi, Z.; Remi, S.; Park, H. S.; Swan, A. K.; Goldberg, B. B. How graphene slides: measurement and theory of strain-dependent frictional forces between graphene and SiO2. *Nano Lett.* **2013**, *13*, 2605−2610.
(76) He, K.; Poole, C.; Mak, K. F.; Shan, J. Experimental demonstration of continuous electronic structure tuning via strain in atomically thin MoS2. *Nano Lett.* **2013**, *13*, 2931−2936.
(77) Plechinger, G.; Castellanos-Gomez, A.; Buscema, M.; Van Der Zant, H. S.; Steele, G. A.; Kuc, A.; Heine, T.; Schueller, C.; Korn, T. Control of biaxial strain in single-layer molybdenite using local thermal expansion of the substrate. *2D Mater.* **2015**, *2*, 015006.
(78) Li, T. Ideal strength and phonon instability in single-layer MoS 2. *2D Mater.* **2012**, *85*, 235407.
(79) Dadgar, A.; Scullion, D.; Kang, K.; Esposito, D.; Yang, E.; Herman, I.; Pimenta, M.; Santos, E.-J.; Pasupathy, A. Strain engineering and Raman spectroscopy of monolayer transition metal dichalcogenides. *Chem. Mater.* **2018**, *30*, 5148−5155.
(80) Sahin, H.; Tongay, S.; Horzum, S.; Fan, W.; Zhou, J.; Li, J.; Wu, J.; Peeters, F. Anomalous Raman spectra and thickness-dependent electronic properties of WSe 2. *Phys. Rev. B* **2013**, *87*, 165409.
(81) Hod, O.; Meyer, E.; Zheng, Q.; Urbakh, M. Structural superlubricity and ultralow friction across the length scales. *Nature* **2018**, *563*, 485−492.
(82) van der Zande, A. M.; Kunstmann, J.; Chernikov, A.; Chenet, D. A.; You, Y.; Zhang, X.; Huang, P. Y.; Berkelbach, T. C.; Wang, L.; Zhang, F.; Hybertsen, M. S.; Muller, D. A.; Reichman, D. R.; Heinz, T. F.; Hone, J. C. Tailoring the Electronic Structure in Bilayer Molybdenum Disulfide via Interlayer Twist. *Nano Lett.* **2014**, *14*, 3869−3875.
(83) Janssen, G. C.; Abdalla, M.; Van Keulen, F.; Pujada, B.; Van Venrooy, B. Celebrating the 100th anniversary of the Stoney equation for film stress: Developments from polycrystalline steel strips to single crystal silicon wafers. *Thin Solid Films* **2009**, *517*, 1858−1867.

https://doi.org/10.1021/acsnano.3c09354
ACS Nano XXXX, XXX, XXX−XXX